

# Brain blood vessel segmentation using line-shaped profiles

Danilo Babin\*, Aleksandra Pižurica, Jonas De Vylder,  
Ewout Vansteenkiste, Wilfried Philips

E-mail: [dbabin@telin.ugent.be](mailto:dbabin@telin.ugent.be)

Department of Telecommunications and Information Processing  
-TELIN-IPI-iMinds, Faculty of Engineering, Ghent University,  
Sint-Pietersnieuwstraat 41, B-9000 Ghent, Belgium.

## Abstract.

Segmentation of cerebral blood vessels is of great importance in diagnostic and clinical applications, especially for embolization of cerebral aneurysms and arteriovenous malformations (AVM). In order to perform embolization of the AVM, the structural and geometric information of blood vessels from 3-D images is of utmost importance. For this reason, the in-depth segmentation of cerebral blood vessels is usually done as a fusion of different segmentation techniques, often requiring extensive user interaction. In this paper we introduce the idea of line-shaped profiling with an application to brain blood vessel and AVM segmentation, efficient both in terms of resolving details and in terms of computation time. Our method takes into account both local proximate and wider neighbourhood of the processed pixel, which makes it efficient for segmenting large blood vessel tree structures, as well as fine structures of the AVMs. Another advantage of our method is that it requires selection of only one parameter to perform segmentation, yielding very little user interaction.

*Keywords:* Image segmentation, cerebral blood vessels, multi-orientation profiles.  
Submitted to: *Phys. Med. Biol.*

\* Corresponding author

## 1. Introduction

This paper introduces the segmentation principle of line-shaped profiles, building on our previous work on generalized profiling (GP) (Babin et al. 2012). Segmentation and visualization of brain blood vessels is essential in clinical practice for diagnostics and surgery. Examining the structure and configuration of vessels is especially important in embolization (a surgery to insert coils or glue for making occlusion in the aneurysm or the arteriovenous malformation (AVM)). For surgical planning of the AVM embolization, an interest is taken both in the fine segmentation of the cerebral blood vessel tree and structure delineation between feeding arteries, the draining vein and the nidus of the AVM. Beside the exact AVM geometry and volume calculation, computational efficiency is also an important requirement. In this paper we seek a solution to the problem of accurate and detailed segmentation of a cerebral blood vessel tree with an AVM. Based on the current reviews of vessel extraction techniques (Kirbas & Quek 2004, Lesage et al. 2009, Yaniv & Cleary 2006), we classify the existing methods for AVM extraction into visualization and segmentation methods.

The goal of the visualization is to enhance the existing blood vessel images in order to aid a surgeon in decision making and surgery. However, blood vessel models are not explicitly generated (as in segmentation). Hence, computational analysis of the blood vessel structure and the best path calculations are not possible.

Visualization is performed either by application of advanced image processing and computer graphics methods or by using multiple imaging modalities and acquisitions (multiple data sets acquired by a single modality).

A large number image processing studies treat visualization of cerebral aneurysms and malformations, as well as blood vessels of brain in general (Antiga & Steinman 2006, Bullitt et al. 2001, Coenen et al. 2005, Forkert et al. 2009, Piccinelli et al. 2009). However, these visualizations are usually not capable of fine delineation between the feeding arteries, draining vein and nidus, which is exactly the focus of this work. The approach of (Qian et al. 2009) examines the polar neighbour intensity profile of a voxel in order to determine a “vesselness measure” for characterizing vascular structures. The vesselness measure is usually obtained on the basis of eigenvalues of the Hessian as in (Frangi et al. 1998, Jackowski et al. 2005), where an assumption is used that a single cylinder exists around each voxel. However, the vesselness measure is hard to determine in case of complex AVM structures. Diffusion tensor (DT) fibre tractography has also been applied in AVM examination and is more suitable for therapeutic stages (Okada et al. 2007).

Multiple imaging approach of (Säring et al. 2007) combine 3-D and 4-D MR image sequences to visualize and analyse malformations. Digital subtraction angiography (DSA) methods (Coste et al. 2001, Söderman et al. 2000) have proven crucial in AVM related surgery (Zhang et al. 2003), and validation methods for this imaging modality have also been developed (Berger et al. 2008). However, DSA methods (Coste et al. 2001, Söderman et al. 2000), while efficient in determining volume of the AVM, are not able to delineate the inner structure of the malformation.

The goal of a blood vessel segmentation is to provide a surgeon with a blood vessel tree model. The difference with visualization techniques is that the structure of the resulting model can be analysed to provide valuable vessel information (e.g. vessel radii, bending angles and the best paths). The segmentation of blood vessels is a difficult task in general, because of a varying structure, size and direction of blood vessels in a 3-D image and these problems escalate in the case of the

AVM segmentation, because of its highly unpredictable structure. Therefore, prior knowledge concerning the position of blood vessels and even their number in the malformation is limited. Simple approaches as adaptive thresholding and connected components methods (Carrillo et al. 2005, De Bock & Philips 2010) have difficulties in dealing with high variety of pixel intensities. Active contours (Shang et al. 2008, Shang et al. 2011) give good results when segmenting blood vessels in images of sufficient resolution, which is not the case in AVM segmentation. Shape and flow driven methods optimized for segmenting tubular structures (Pechaud et al. 2009, Cebral et al. 2005, Castro & Cebral 2007, Hoi et al. 2004, Nain et al. 2004) are able to segment vessels going in or out of the malformation, but are not applicable for segmenting complex structure (such as the nidus of the malformation) at lower resolutions. The atlas-based methods (Passat et al. 2005) or methods incorporating anatomical prior knowledge (Passat et al. 2006) show good results for segmenting non-malformed vessels of the cerebral blood vessel tree. However, the prior knowledge concerning the AVM anatomy is limited, due to its unpredictable structure. Vessel segmentation methods based on centreline and path extraction (Dokladal et al. 1999, Wesarg & Firlé 2004) extract centrelines either from an existing segmentation model or from ridges in the original image. Segmentation-based centreline extraction methods rely on the segmentation algorithm used, while ridge-based methods have difficulties with pixel intensity inhomogeneities in the AVM. Methods based on deformable models (Caselles et al. 1995, Lorigo et al. 2001) are able to segment even smaller blood vessels, but the parameters are highly dependent on pixel intensity distribution, which can result in incorrect thickness of segmented vessels.

The idea of line-shaped profiles is based on our previous work on generalized profiling (GP) (Babin et al. 2012), as an extension of morphological profiles (Pesaresi & Benediktsson 2001, Plaza et al. 2004, Bellens et al. 2008). Morphological profiles introduce comparisons between morphological operations with different size of the structuring element (SE). In (Babin et al. 2009, Babin et al. 2012), we extended the idea of morphological profiles by introduction of more complex ring-shaped SEs and various operators applied to the SE (as an alternative to minimum and maximum operators in morphological profiles). In this work we further extend this idea and define novel orientation-based structuring elements. The use of line-shaped SE, as one of our main novelties, transforms the idea of multi-scale approach into a multi-orientation approach, which enhances the computational efficiency and shortens execution times. Another important novelty in this work is the introduction of second order operators as operators applied on the set of calculated operator values (instead only on a set of pixels defined by the SE, as in (Babin et al. 2012)), yielding higher segmentation quality results. We base our segmentation principle on comparing the values of pixels with the characteristic values of their neighbourhoods defined by differential SEs. This way, the method is quite robust to local variations in pixel intensities and is governed by the user defined operator for calculating the characteristic of the neighbourhood. We design a method for evaluation of profile operators based on their average values, which allows a user to easily perform segmentation by adjusting only one parameter.

## 2. The proposed method

### 2.1. Previous work

The approach presented in this paper is related to our previous work on generalized profiling (GP) (Babin et al. 2012) and to morphological profiles (MP) (Pesaresi & Benediktsson 2001, Plaza et al. 2004). Both approaches are multi-scale methods that make use of a 2-D structuring element (SE)  $S_n(\mathbf{p})$  as a 2-D window of a certain shape and size  $n$  centred at the point  $\mathbf{p}$ .

One of the main differences between our method described in (Babin et al. 2009, Babin et al. 2012) and the morphological profiles is that we used a ring-shaped structuring element defined as a difference of two classical structuring elements  $S(\mathbf{p})$  of different size, which we call a *differential structuring element* (DSE)  $D_{r,n}(\mathbf{p})$ :

$$D_{r,n}(\mathbf{p}) = S_{r+n}(\mathbf{p}) \setminus S_r(\mathbf{p}), \quad r \in \{0, 1, \dots\}, \quad n \in \mathbb{N}. \quad (1)$$

Figure 1a shows circular and rectangular DSEs of different parameters. For these shapes, different parameters indicate a change in size and for that reason we call them *size-based* structuring elements. Another important innovation in (Babin et al. 2012) was the introduction of a *profile operator*  $f$  as an arbitrary operator on the multi set of grey pixel values contained in the DSE, which we call *windowed pixel intensities*. Let  $D'_{r,n}(\mathbf{p}, g)$  denote a multi set of windowed pixel intensities from an image  $g$  using the DSE  $D_{r,n}$ :

$$D'_{r,n}(\mathbf{p}, g) = \{g(x, y) \mid (x, y) \in D_{r,n}(\mathbf{p})\}. \quad (2)$$

Therefore, the profile operator is an operator applied to the windowed values:

$$f(r, n, \mathbf{p}, g) \equiv f(D'_{r,n}(\mathbf{p}, g)). \quad (3)$$

More general profile operators were generated as a combination of arbitrarily chosen operators called *base profile operators*  $f_{B_i}$ :

$$f = \frac{1}{d} \sum_{i=1}^d f_{B_i}, \quad (4)$$

where  $d$  represents the number of base operators involved in generating the combined operator  $f$ .

In this paper we examine line segments as SE shapes, which yields an *orientation-based* profiling approach.

### 2.2. Line-shaped profiling

The main novelty of this paper is the introduction of line-shaped SE as a set of points on the line stretching through the whole image, as illustrated in figure 1b. In this case only the orientation of the line-shaped SE differs, while the size depends solely on image dimensions. Such SE shapes we call *orientation-based* SEs.

In the case of a 3-D line-shaped SE, we use the SE as a set of pixels in a line defined by the direction vector dependent on the parameter  $n$  and a pixel  $\mathbf{p} = (x, y, z)$  on the line:

$$L_n(\mathbf{p}) = \{\mathbf{p} + t\mathbf{k}(n) \mid t \in \mathbb{R}\}, \quad (5)$$

where  $\mathbf{k}(n)$  denotes the unit vector that determines the line segment direction from a set of predefined direction unit vectors ( $n \in [1, n_{max}]$ ). This yields  $n_{max}$  number

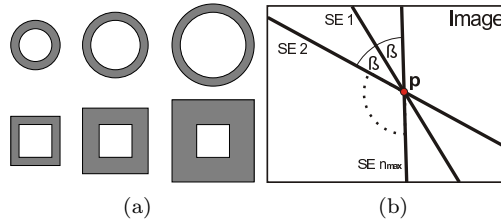


**Figure 1.** (a) Examples of differential structuring elements (DSEs) from (Babin et al. 2012), which define a multi-scale approach. (b) Multi-orientation approach with line-shaped (orientation-based) SEs is a novelty introduced in this paper. Each of the  $n_{max}$  SEs is represented by a line, limited by the image size. The illustration shows a 2-D slice, although our proposed method works in 3-D space.

of line-shaped SEs, which we distribute uniformly in the 3-D space. An important observation is that the line-shaped SE differs from size-based SEs by introduction of parameter  $n$  which controls its orientation.

As in (Babin et al. 2012) we introduce a *profile operator*  $f$  as an arbitrary operator on the window defined by the SE. Let  $L'_n(\mathbf{p}, g)$  denote a multi set of windowed pixel intensities from an image  $g$  using the line-shaped SE  $L_n$ :

$$L'_n(\mathbf{p}, g) = \{g(\mathbf{p}') \mid \mathbf{p}' \in L_n(\mathbf{p})\}. \quad (6)$$

Therefore, the profile operator is an operator applied to the windowed values:

$$f(n, \mathbf{p}, g) \equiv f(L'_n(\mathbf{p}, g)). \quad (7)$$

In our previous work (Babin et al. 2009) we used an average operator applied to the DSE as an alternative to using minimum and maximum applied in morphological profiles. As in (4), a more general profile operator is obtained as combination of arbitrarily chosen base profile operators.

In this paper we use the following base operators: *avr* (average), *min* (minimum) and *max* (maximum). The listed operators have proven effective for segmentation in our experiments, although the user may specify any other operator (defined on a set of values) as well, where the total number of operators is also user defined (e.g. median can also be used as a base profile operator, but we avoid its use due to required array sorting which prolongs execution times). Later in the work we will introduce a simple method for selecting the optimal profile operator  $f$  (as a combination of available base profile operators  $f_B$ ) for segmentation purposes and explain why our choice of base operators falls on the mentioned ones. The advantage of this approach is that by combining different base operators into complex ones, we obtain a qualitatively wider range of segmentation results, and we design an efficient way for the user to easily select the optimal one, which we describe in Section 2.5.

In case of a line as a SE, only the orientation parameter is relevant. Hence, we represent the line profile of an operator  $f$  as a vector named *L-Profile*,  $\mathbf{l}_f(\mathbf{p}, g)$  by varying line SE orientation  $n$ :

$$\mathbf{l}_f(\mathbf{p}, g) = (f(n, \mathbf{p}, g) \mid n \in [1, \dots, n_{max}]). \quad (8)$$

The main advantage of lines as strictly orientation-based SEs is that the minimum, maximum and average base operators are easily calculated for all the pixels belonging to a single line, yielding short computation times. However, large SEs are used for profile operators, which raises questions about their usability for image analysis

(consequently, the quality of segmentation is under question). In order to resolve this problem, later in the paper we propose novel profile operators, which take into account the operator values obtained on sets of SEs, instead on a single SE. These novel operators are called *second order profile operators* and will be further discussed in Subsection 2.4.

Finally, in order to obtain a transformed image we need to assign a single measure to the calculated L-Profiles at each pixel  $\mathbf{p}$  of the image. In (Babin et al. 2012) we compared a pixel intensity with the intensities found in its neighbourhood. The brightness of a pixel was defined as a size of a ring-shaped SE up to which the pixel intensity was higher than the neighbourhood brightness (i.e. the calculated profile operator value). That way the profile measure indicated the size (range) of the bright object to which the processed pixel belongs. However, line-shaped SEs are different in orientation, while the size is always limited by the image dimensions. Similarly to our previous work, we determine the brightness of a pixel by comparing the calculated operator value in a line-shaped SE to the pixel value. For a predefined profile operator, we calculate the number of line-shaped SEs for which the given profile operator value is lower than the processed pixel intensity. In other words, when segmenting bright objects (as in cerebral vessel CTA images), we need the value of the processed pixel  $\mathbf{p}$  to be higher than the operator value calculated on the line-shaped SE  $f(n, \mathbf{p}, g)$ .

In this fashion, we define the *conditional set*  $C$  as a set of all elements of a L-profile with value lower than the processed pixel value  $g(\mathbf{p})$ :

$$C(\mathbf{I}_f(\mathbf{p}, g)) = \{f(n, \mathbf{p}, g) \mid f(n, \mathbf{p}, g) \leq g(\mathbf{p}), n \in [1, \dots, n_{max}]\}. \quad (9)$$

The transformed pixel value  $\lambda$  is equal to the number of L-profile elements for which the predefined condition is met, representing the cardinality of the conditional set  $C$ :

$$\lambda(\mathbf{p}, g) = \text{card}(C(\mathbf{I}_f(\mathbf{p}, g))). \quad (10)$$

In order to obtain the final segmentation, we threshold the transformed image (the image obtained using (9) and (10)). The transformed pixel values fall in range  $[1, \dots, n_{max}]$ , where  $n_{max}$  represents the total number of directions (different SEs) used in L-profile calculation in (8), and the threshold has to be selected from this range. In our case all the directions are of equal importance. Hence, we set the threshold to the highest possible value  $t = n_{max}$ . Segmentation results are shown in figure 2. The original CTA slice is shown in figure 2a with the illustration of line directions (in 2-D slice) for profile calculation. The corresponding transformed image calculated for  $n_{max} = 13$  directions in 3-D space and a user defined profile operator  $f = (\min + \max)/2$  in figure 2b is thresholded with maximal threshold value  $t = n_{max}$  and the final segmentation is depicted in figure 2c.

### 2.3. Optimal number of line directions

Our proposed algorithm performs segmentation by comparing the current pixel to its neighbourhood (defined by the profile operator  $f$ ). By increasing the number of directions (SEs) used, we increase the delineation area (in segmented image) between blood vessel pixels and noisy background. This principle is illustrated (for a 2-D slice) in figure 3 where 4, 8 and 10 directions create circle shaped delineation area with pixel radii 2, 3 and 4, respectively. This means that 10 directions will be sufficient for the line-shaped SEs to pass through every pixel in the circle-shaped neighbourhood with radius of 4 pixels from the processed pixel. The same principle applies to the 3-D case, where the line directions in 3-D create a spherical delineation area. This means

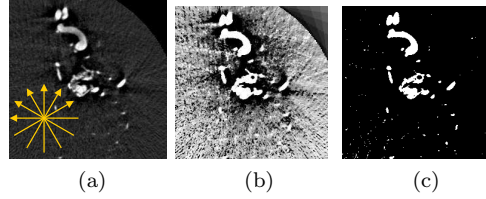


**Figure 2.** Illustration of segmentation using the line-shaped SE. (a) The original slice of the 3-D CTA brain blood vessel image with the illustration of 6 directions of line-shaped SEs for an arbitrary pixel. (b) Transformed image for profile operator  $f = (\min + \max)/2$  and (c) the corresponding segmentation for 13 line directions in 3-D space.

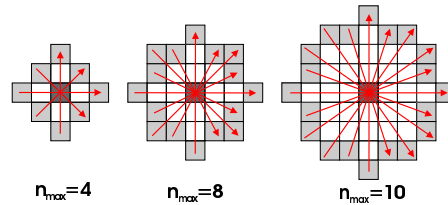


**Figure 3.** Increasing the number of directions increases the number of equidistant pixels covered by the resulting line-shaped SEs and enlarges delineation area between the object and noisy background pixels (4, 8 and 10 directions create circle shaped delineation area with pixel radii 2, 3 and 4, respectively). The same principle applies to the 3-D space, where the line directions in 3-D create a spherical delineation area.

that using line-shaped SEs the segmentation process considers both local proximate and wider neighbourhood of the processed pixel, which is a benefit of our approach.

We determine the optimal number of directions based on the desired delineation area, which we estimate by taking into account the maximum blood vessel size. Experience shows that the delineation area should be at least the size of the maximum vessel radius. However, due to the fast execution of our proposed method, we set the number of directions to a higher value than estimated to ensure a sufficiently large delineation area (in this paper we use  $n_{max} = 45$ ) without significantly prolonging execution times.

Figure 4 shows the influence of contrast and distribution of vessel area (with the constant number of directions  $n_{max} = 45$ ) on segmentation results. The vessel area in the original CTA slice in figure 4a is smaller and more concentrated at a single location in the image compared to the vessels seen in figure 4d. Therefore, more noisy background pixels are segmented in figure 4b than in figure 4e, but these areas are further away from the blood vessel regions (see figure 4b) because of sufficiently high number of directions. Due to the large delineation area, the blood vessels are extracted as the largest connected 3-D region using 3-D binary connectivity filter (see figure 4c and figure 4f).

#### 2.4. Second order profile operators

If we increase the number of directions, the delineation area increases as well. However, this can have a negative impact on segmentation results calculated using

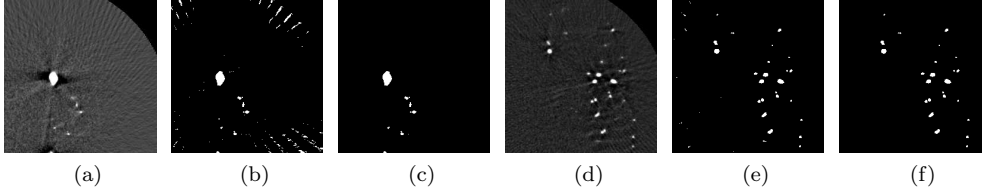


**Figure 4.** Example of segmentation influenced by the area and concentration of vessels (parameters:  $n_{max} = 45$ ,  $f = (\min + avr + \max)/3$ ). (a), (d) The original 3-D CTA slices. (b), (e) Segmentation results before binary connectivity filtering. (c), (f) Final segmentation of vessels (after applying 3-D binary connectivity filtering).

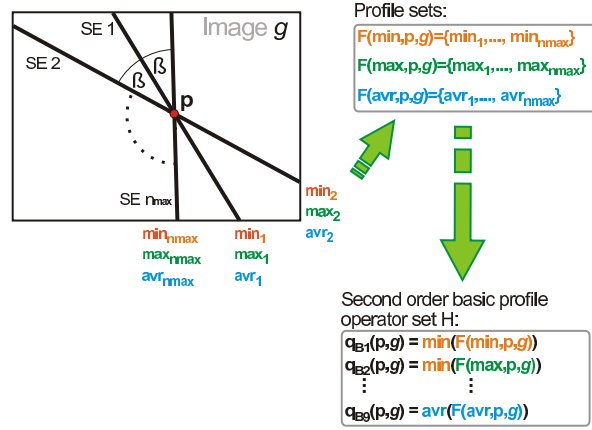


**Figure 5.** The principle behind second order profile operators. For each pixel  $\mathbf{p}$ , and each base profile operator  $f_B$  a profile set  $F(f_B, \mathbf{p}, g)$  is formed. Second order base profile operator  $q_{Bk}(\mathbf{p}, g)$  is an operator  $f_{B_i}$  applied to profile multi set  $F(f_{B_j}, \mathbf{p}, g)$ , where  $k = (i - 1)d + j$  and  $d = \text{card}(B)$ .

profile operators that include minimum and maximum values. This happens due to the proposed segmentation principle, where the current pixel value is compared to calculated profile operator value for all SE directions (see (9) and (10)). In case of minimum as a base profile operator this means that the lowest calculated minimum operator value for all SEs of pixel  $\mathbf{p}$  will determine the segmentation outcome. Similarly, in case of maximum as a base profile operator it will be the highest calculated maximum operator value for all SEs of pixel  $\mathbf{p}$ . This presents a problem because by increasing the number of directions the lowest minimum profile operator value will converge towards the minimum value of the whole image (because the minimum value decreases as the number of pixels taken into account increases). Hence, the calculated lowest minimum value is not an operator of the pixel neighbourhood any more (due to the large SE), but of the whole image (and, therefore, it will have an approximately constant value for each pixel in the image). The same reasoning can be applied for the maximum as a profile operator where the highest maximum profile operator value converges towards the maximum value of the whole image. In order to preserve the dependency of the profile operator values from the pixel neighbourhood, we propose a method to create new base operators from the existing ones, as illustrated in figure 5.

We define the *profile multi set*  $F(f_B, \mathbf{p}, g)$  of a pixel  $\mathbf{p}$  and base profile operator  $f_B$  as a multi set of base profile operator values  $f_B(n, \mathbf{p}, g)$  calculated for all SEs of processed pixel  $\mathbf{p}$ :

$$F(f_B, \mathbf{p}, g) = \{f_B(n, \mathbf{p}, g) \mid n \in [1, \dots, n_{max}]\}. \quad (11)$$

Note that the profile multi set  $F(f_B, \mathbf{p}, g)$  represents in fact the multi set of vector components of L-profile as defined in (8), where the profile operator is a base profile operator  $f_B$ . To extend the set of values calculated by base profile operators we define the *second order base profile operator*  $q_{Bk}(\mathbf{p}, g)$  of a pixel  $\mathbf{p}$  as a base profile operator  $f_{B_i}$  applied to the profile multi set  $F(f_{B_j}, \mathbf{p}, g)$ :

$$q_{Bk}(\mathbf{p}, g) \equiv f_{B_i}(F(f_{B_j}, \mathbf{p}, g)), \quad i, j \in [1, \dots, d], \quad k = (i - 1)d + j, \quad (12)$$

where  $d = \text{card}(B)$  is the number of base profile operators. The set of all base second order profile operators for a pixel  $\mathbf{p}$  we call the *second order base profile multi set*  $H(\mathbf{p}, g)$ , which is in fact a multi set of all base profile operators applied to all profile multi sets  $F(f_B, \mathbf{p}, g)$ :

$$H(\mathbf{p}, g) = \{q_{Bk}(\mathbf{p}, g) \mid k \in [1, \dots, d^2]\}. \quad (13)$$

The second order profile multi set  $H(\mathbf{p}, g)$  for base operator set  $B = \{\text{min}, \text{avr}\}$  will consist of the following operator values:  $\text{min}(F(\text{min}, \mathbf{p}, g))$ ,  $\text{min}(F(\text{avr}, \mathbf{p}, g))$ ,  $\text{avr}(F(\text{min}, \mathbf{p}, g))$  and  $\text{avr}(F(\text{avr}, \mathbf{p}, g))$ . Obviously, for  $d$  base profile operators, the second order profile multi set  $H(\mathbf{p}, g)$  will consist of  $d^2$  different operator values. Let us denote a  $k$ -th second order base profile operator from the set  $H(\mathbf{p}, g)$  with  $q_{Bk}$ . Similarly to (4), a more complex second order profile operator value  $q(\mathbf{p}, g)$  is created as a combination of values in  $H(\mathbf{p}, g)$ :

$$q(\mathbf{p}, g) = \frac{1}{u} \sum_k q_{Bk}(\mathbf{p}, g), \quad q_{Bk}(\mathbf{p}, g) \in H(\mathbf{p}, g), \quad (14)$$

where  $u$  is the number of second order base profile operators involved in creating a more complex profile operator  $q$ . Since the second order base operators already take into account base profile operators calculated on different SEs of a single pixel, the transformed pixel value is simply the value of the profile operator  $q(\mathbf{p}, g)$ :

$$\lambda(\mathbf{p}, g) = q(\mathbf{p}, g). \quad (15)$$

As before, the final segmentation is obtained by thresholding the original pixel value with its transformed value.

### 2.5. Evaluation of profile operators

Second order profile operators take into account the pixel intensity distribution in a wider pixel neighbourhood. For a given base operator set  $B$ , we can obtain  $2^{\text{card}(B)^2} - 1$  different second order operators, and hence, different segmentation results (thresholding is performed by comparison of the transformed pixel value with its original intensity, as discussed earlier). However, in case of cerebral AVM CTA images, we need to determine a way to estimate the performance of each operator to be able to select the optimal one. The AVM has such an unpredictable structure that we do not have sufficient criteria to evaluate the vessel segmentation result (there is no clear vessel radius, curvature, connectedness or structure to relate to). Instead, we will examine an average profile operator value in the 3-D image for each of the profile operators. By comparing the average values of profile operators we can estimate (in a

comparative manner) the overall number of pixels which will be segmented. In other words, by ordering average profile operator values, we can determine which operator will result in a larger segmented volume in the final segmentation. Based on the obtained order, the optimal profile operator is manually selected in an easily to use “threshold selection” manner.

In order to define the criteria for evaluating different second order profile operators  $q$ , we define the average base profile operator value  $\overline{q_{Bk}}$ :

$$\overline{q_{Bk}}(g) = \frac{1}{m} \sum_{\mathbf{p}} q_{Bk}(\mathbf{p}), \quad (16)$$

where  $m$  represents the number of pixels in the 3-D image. Since the profile operator  $q$  is generated as a combination of base profile operators, we obtain its average value in an analogous way (which means that it does not need to be recalculated for each profile operator separately):

$$\overline{q}(g) = \frac{1}{u} \sum_k \overline{q_{Bk}}(g). \quad (17)$$

By comparing and sorting the calculated average second order profile operator values  $\overline{q}(g)$  we create a “threshold selection” type segmentation approach (with a difference that the “threshold” in our case refers to an operator and not a single pixel value). From this information, it is easy to determine which operator should be used if the segmented object area needs to be altered (e.g. for larger areas the operators with the lower average value should be chosen). In practice, all the possible operator values are sorted according to the calculated values and the operator selection is performed as a simple “threshold” value selection, which is an accepted and desired concept in clinical image analysis.

## 2.6. Algorithm overview and application

Figure 6 shows the block diagram of the line-shaped SE profiling using second order profile operators, as proposed in Sections 2.4 and 2.5. The result of thresholding (in an optional preprocessing step) can be used as a mask for the proposed algorithm. The algorithm starts by calculating base second order operators for each voxel of a 3-D image for 45 line directions in a 3-D space (ensuring the sphere delineation area radius of 4 voxels, which is enough for CTA images of cerebral blood vessels). In the third step of the algorithm, the average base second order profile operators  $\overline{q_{Bk}}(g)$  are calculated (16). From these, the average value of each second order profile operator  $\overline{q}(g)$  is computed (17). The computed values are sorted in an ascending order and will be used to aid in selecting the optimal profile operator for segmentation. The ordered array of second order profile operators represents threshold-type order. In the fourth step the user selects the second order profile operator. By default we set it to be the operator with the median average profile value of all calculated average profile values. In the final step the segmentation is obtained by thresholding the calculated transformed value with the original pixel value.

If the user is not satisfied with the segmentation result, another second order profile operator can be selected and the segmentation repeated (the last 2 steps of the algorithm). By inspecting the obtained segmentation, the user can select a new profile operator in the following fashion. If the vessels have been undersegmented, a second order operator with lower average value has to be selected. Similarly, if the vessels

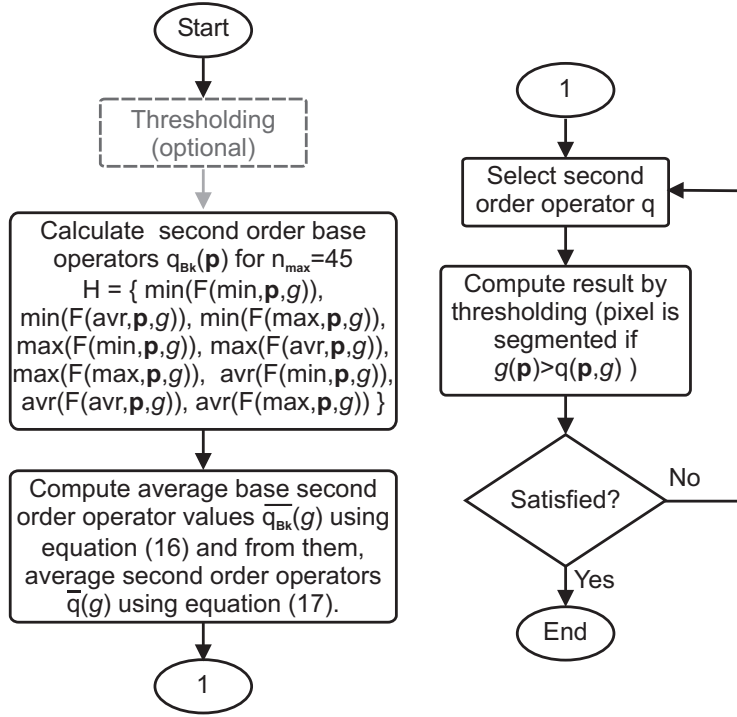


Figure 6. Block diagram of the algorithm using second order profile operators.

have been oversegmented, a second order operator with higher average value has to be selected. This is performed in matter of seconds. An advantage of our approach is that L-profiles do not need to be recalculated.

It should be emphasized that the only parameter that a user has to select is the second order profile operator (which is performed in a simple “threshold selection” type manner).

An important advantage of using orientation-based SEs over size-based SEs is a higher computational efficiency. This is caused by the fact that values of base profile operators are identical (equal) for all pixels in the line-shaped SE. Hence, there is no need of recalculating values of base operators for each pixel in the line-shaped SE. Since the line-shaped SE can be a large window, it is of interest to use operators for which the result can be calculated by a single pass through windowed values. Therefore, we use average, minimum and maximum operator in our experiments.

### 3. Results

In order to compare various segmentation methods, we use phantom data and real CTA data sets of cerebral blood vessels in our experiments.

#### 3.1. Segmentation of phantom data

For evaluating the combined profile operators we have generated three 3-D phantom cerebral blood vessel tree data sets (each 3-D set consists of around 200 slices, see

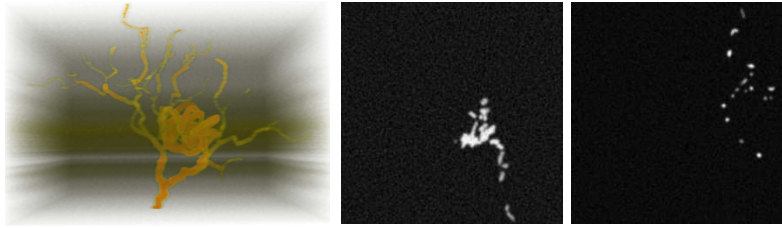


**Figure 7.** Vessel tree phantom data set after adding noise and CT artefacts (176 slices with resolution of  $256 \times 256$  pixels). Left: volume rendering of the whole data set, centre and right: slices from the data set.

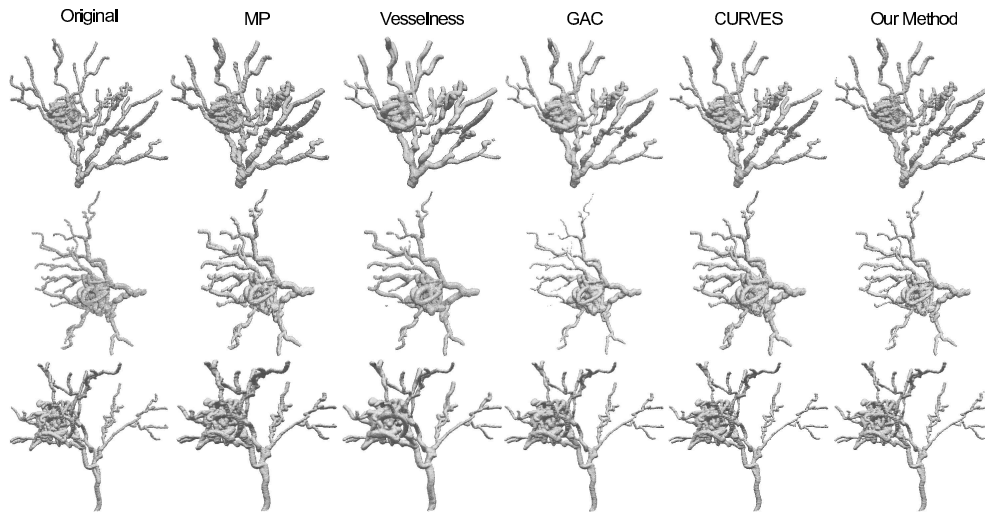


**Figure 8.** Comparison between different segmentation techniques on 3-D phantom data representing binary tree with AVM. The results are organized in columns sorted from left to right: (column 1) original phantom models, (column 2) morphological profiles (MP) (Pesaresi & Benediktsson 2001), (column 3) vesselness measure (Jackowski et al. 2005), (column 4) geodesic active contours (GAC) (Caselles et al. 1995), (column 5) curve evolution for vessel segmentation (CURVES) (Lorigo et al. 2001) and (column 6) our proposed method (block diagram in figure 6).

figure 7) and three 3-D phantom AVM data sets. The 3-D phantom model data sets of cerebral blood vessel tree represent a binary tree with a random branch distribution, and with a random shape and thickness corresponding to the random structure of an AVM. The phantom tree models are tubular structures with random curvatures and tube radii, while the AVM part of the phantom is intertwined in a random way to simulate the unpredictable structure of the AVM nidus, as shown in the first column of figure 8. The 3-D AVM phantom data sets are models of randomly intertwined tubular structure with randomly varying radii. In order to obtain realistic CT images with noise, streaking artefacts and blurring were added. The images were transformed to sinogram space (using a sufficiently large number of projection angles) and the inverse logarithmic transform is applied to obtain the raw detector signal. Overlap of neighbouring detector element responses is simulated through a Gaussian blurring

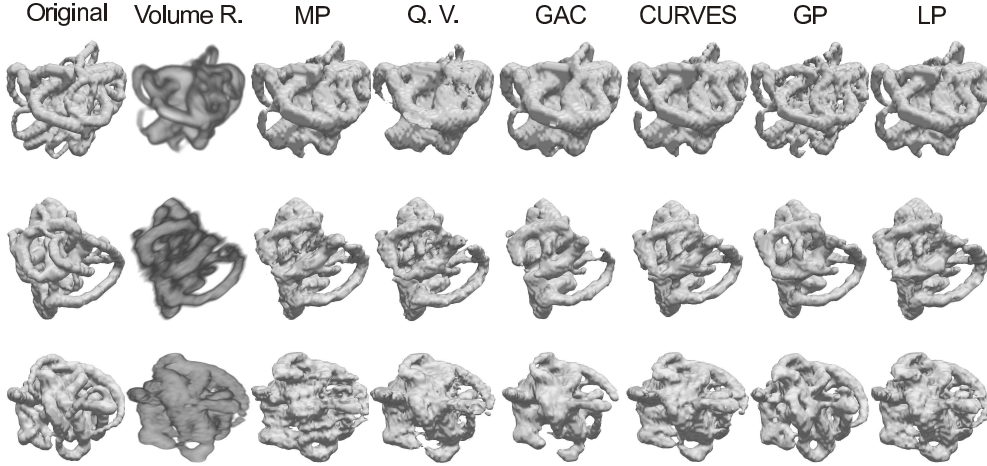


**Figure 9.** Comparison between different segmentation techniques on 3-D AVM phantoms. The results are sorted in columns from left to right: original AVM phantom model, volume rendering of the model with CT artefacts, morphological profiles (MP) (Pesaresi & Benediktsson 2001), vesselness measure (Qian et al. 2009), geodesic active contours (GAC) (Caselles et al. 1995), curve evolution for vessel segmentation (CURVES) (Lorigo et al. 2001), generalized profiles (Babin et al. 2012) and our proposed method.

**Table 1.** Calculated Dice coefficients for comparison of various segmentation methods applied to the phantom data

Dice	$a = 2^9, \sigma = 0.9$	$a = 2^{10}, \sigma = 0.8$	$a = 2^{11}, \sigma = 0.6$
MP	0.687	0.681	0.7
GAC	0.762	0.801	0.868
CURVES	0.799	0.844	0.892
Vesselness	0.701	0.715	0.787
GP	0.732	0.78	0.802
LP (eqn. (10))	0.771	0.862	0.86
LP	0.874	0.897	0.902

operation of the data along the detector array. Poisson noise is added to the filtered data, in order to simulate the x-ray photon arrival process. Finally, the forward logarithmic transform is applied and the resulting sinograms are backprojected by the filtered backprojection algorithm using the ramp filter. For each of the data sets the parameters simulating radiation quantity  $a$  (which is a signal amplitude, inverse to noise level) and blurring  $\sigma$  were set to different values. A vessel tree phantom data set is depicted in figure 7. For evaluating the obtained results we use the Dice coefficient (Dice 1945), which is a set similarity measure defined as twice the ratio of intersection of two sets and the number of elements contained in both of them:

$$s(A, B) = \frac{2|A \cap B|}{|A| + |B|}, \quad (18)$$

where one set indicates the set of segmented pixels and the other one the set of ground truth pixels.

Results obtained on the cerebral blood vessel tree phantom data are shown in figure 8, where ground truth phantom models are visualized in the first column, followed by the segmentation models obtained using the classical MP (Pesaresi & Benediktsson 2001), vesselness measure (Jackowski et al. 2005, Papademetris et al. n.d.), geodesic active contours (GAC)(Caselles et al. 1995), curve evolution for vessel segmentation (CURVES) (Lorigo et al. 2001), the generalized profiling (GP) (Babin et al. 2012), our proposed method as given in (10) and our proposed method using the second order profile operators (block diagram in figure 6). The GAC and CURVES segmentation was obtained using Vascular Modeling Toolkit (VMTK) (Antiga & Steinman 2006) in 3D Slicer (Pieper et al. 2006), with manually set seed points. Results of our proposed method (depicted in the last column of figure 8) show the best delineation of the tubular structure of the phantom and the complex AVM phantom structure, while most of the other segmentation methods segment individual vessels well, but either remove significant parts of the AVM phantom, or merge them into a single region. This is confirmed by the calculated Dice coefficients shown in table 1, which have the highest values for our proposed method with second order profile operators (block diagram in figure 6) for each phantom data set. Method with ordinary profile operators (the transformed pixel value is defined in (10)), results in Dice coefficients lower than for the CURVES algorithm, but higher than the GAC method. With this we prove the benefit of introducing the second order profile operators.

To evaluate our proposed algorithm for the segmentation of AVM vessels, we design three 3-D phantom data sets of highly intertwined tubular structure of varying radii. CT radiation quantity  $a$  and blurring  $\sigma$  were set to different values for each data set. Figure 9 shows the segmentation results for various segmentation methods. The original AVM phantom models and their corresponding CT data volume renderings are shown in the first two columns. The results of the following methods are shown: morphological profiles (MP) (Pesaresi & Benediktsson 2001), vesselness measure (Q. V.) (Qian et al. 2009, Papademetris et al. n.d.), geodesic active contours (GAC)(Caselles et al. 1995), curve evolution for vessel segmentation (CURVES) (Lorigo et al. 2001), generalized profiles (GP) (Babin et al. 2012) and our proposed method (LP) as in the block diagram in figure 6. Tubular AVM structure is delineated the best using the generalized profiles (GP) approach. However, this approach is not as suitable for skeleton extraction, because the method is sensitive to noise. The results of our proposed line-shaped profiling (LP) show that the method is more robust to noise, while still delineating major vessels well. The other methods have a tendency to merge AVM vessels and give no information on the inner AVM structure. This is supported by the Dice coefficients in table 2, where our proposed algorithm has the highest scores of all other methods. Table 3 shows percent errors for volumes of segmented models in comparison to the volume of the ground truth. The proposed algorithm gives the best scores for the least blurred images, but also estimates well the volume of other AVM phantoms. Finally, we use the Hausdorff distance as a measure of distance between two sets:

$$d_H(A, B) = \max(\sup_{\forall b \in B} \inf_{\forall a \in A} (d(a, b)), \sup_{\forall a \in A} \inf_{\forall b \in B} (d(a, b))) \quad (19)$$

where one set indicates the set of segmented pixels and the other one the set of ground truth pixels. Table 4 presents the Hausdorff distance values for the obtained segmentation models, where our proposed algorithm gives the best results (on average) when compared to other methods.

**Table 2.** Calculated Dice coefficients for comparison of various segmentation methods applied to the AVM phantom data

Dice	$a = 2^9, \sigma = 1.9$	$a = 2^{10}, \sigma = 2.1$	$a = 2^{11}, \sigma = 1.7$
MP	0.753	0.796	0.854
GAC	0.819	0.795	0.794
CURVES	0.831	0.799	0.87
Q. V.	0.777	0.768	0.743
GP	0.826	0.819	0.882
LP	0.853	0.832	0.883

**Table 3.** Calculated volume percent errors for comparison of various segmentation methods applied to the AVM phantom data

Vol. % error	$a = 2^9, \sigma = 1.9$	$a = 2^{10}, \sigma = 2.1$	$a = 2^{11}, \sigma = 1.7$
MP	17.5	16.05	18.58
GAC	3.96	3	47.4
CURVES	27.18	39.86	17.36
Q. V.	20.17	26.08	29.6
GP	15.19	14.67	7.73
LP	8.3	16.3	8.1

**Table 4.** Calculated Hausdorff distances for comparison of various segmentation methods applied to the AVM phantom data

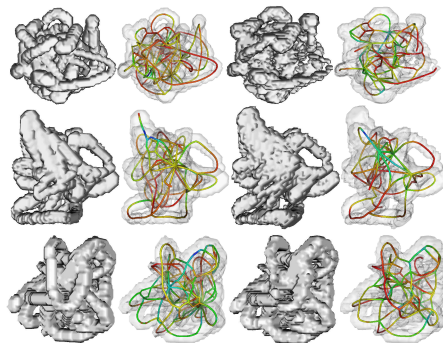
Hausdorff	$a = 2^9, \sigma = 1.9$	$a = 2^{10}, \sigma = 2.1$	$a = 2^{11}, \sigma = 1.7$
MP	4.12	4.35	2.44
GAC	14.86	6.48	2.82
CURVES	7.21	3.6	4.24
Q. V.	8.06	4.35	6.4
GP	4	5	4.12
LP	6.4	4.12	3.6

To compare our proposed algorithm with the generalized profiles (GP) method (Babin et al. 2012), we design 15 additional phantom AVM data sets with varying CT radiation  $a$  and blurring  $\sigma$  parameters. Table 5 shows the Dice coefficient values for our proposed method using second order line-shaped profiles (LP) and generalized profiling (GP) as described in (Babin et al. 2012). The obtained results show higher Dice coefficient values when the line-shaped profiling is used. The phantom data sets used for this comparison are included as supplementary material with this paper.

Figure 10 illustrates the results of skeletonization (Babin et al. 2008) for the original AVM phantoms and the corresponding LP segmentation results, where the skeleton is coloured according to calculated vessel radii. Skeletons obtained from the proposed segmentation algorithm are simplified in the inner AVM regions compared to the skeletons of original models, while maintaining the correct information on AVM structure. This allows us to efficiently determine the best paths in the AVM, used to navigate the catheter in the embolization procedure on the AVM.

**Table 5.** Calculated Dice coefficients for comparison of segmentation using second order line-shaped profiles (LP) and generalized R-profiling (GP).

Dice	LP	GP
$a = 2^9, \sigma = 1.7$	0.872	0.818
$a = 2^9, \sigma = 1.8$	0.86	0.803
$a = 2^9, \sigma = 1.9$	0.854	0.781
$a = 2^9, \sigma = 2.0$	0.839	0.763
$a = 2^9, \sigma = 2.1$	0.84	0.764
$a = 2^{10}, \sigma = 1.7$	0.877	0.871
$a = 2^{10}, \sigma = 1.8$	0.857	0.801
$a = 2^{10}, \sigma = 1.9$	0.855	0.831
$a = 2^{10}, \sigma = 2.0$	0.84	0.813
$a = 2^{10}, \sigma = 2.1$	0.84	0.807
$a = 2^{10}, \sigma = 1.7$	0.874	0.868
$a = 2^{10}, \sigma = 1.8$	0.877	0.859
$a = 2^{10}, \sigma = 1.9$	0.85	0.843
$a = 2^{10}, \sigma = 2.0$	0.848	0.841
$a = 2^{10}, \sigma = 2.1$	0.84	0.829

**Figure 10.** Comparison of skeletons obtained from the ground truth models and from segmented models of phantom AVMs. Columns from left to right: original AVM phantom model, skeleton of the original model, segmented model of AVM phantom using our proposed algorithm and the skeleton of the segmented volume. Skeleton colour mapping indicates calculated vessel radii. Original skeletons and skeletons obtained from the segmentation show good correspondence in outer vessel regions. The inner regions are simplified in the skeletons obtained from the segmentation, which makes it possible to extract larger vessels from the inside of the AVM.

### 3.2. CTA data segmentation

We apply the presented method of profiling using line-shaped SEs for segmentation of 3-D CTA images of brain blood vessels with spacing between slices of 0.62mm and pixel spacing of 0.62mm $\times$ 0.62mm (the resolution of the images is 256  $\times$  256 with around 230 slices in each data set). The results obtained by volume rendering, morphological profiles (MP) (Pesaresi & Benediktsson 2001), vesselness measure (Jackowski et al. 2005, Papademetris et al. n.d.), geodesic active contours (GAC)(Caselles et al. 1995), curve evolution for vessel segmentation (CURVES) (Lorigo et al. 2001) and our

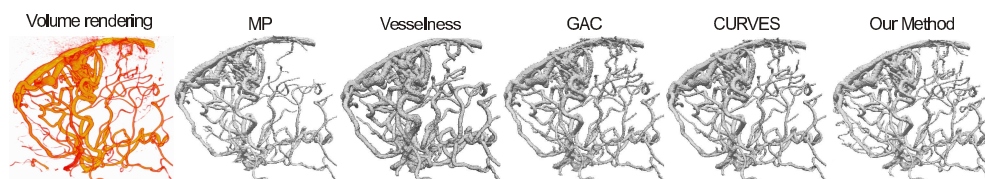


**Figure 11.** Different segmentation techniques applied to 3-D CTA images of brain blood vessels. The depicted results are obtained using volume rendering, morphological profiles (MP) (Pesaresi & Benediktsson 2001), vesselness measure (Jackowski et al. 2005), geodesic active contours (GAC) (Caselles et al. 1995), curve evolution for vessel segmentation (CURVES) (Lorigo et al. 2001) and our proposed method, respectively.

proposed method (block diagram in figure 6) are given in figure 11, respectively. The volume rendering of the data set is given as an evaluation guideline to show the quantity of blood vessels present in the image. The MP methods show poor segmentation of the blood vessel tree because the segmented regions are not connected in 3-D. The vesselness measure produces smooth results, with a bit more structure segmented than with the MP method. GAC result shows even more segmented structure, but with a high impact of noise to the segmentation. Although CURVES give a visually nice segmentation result with high amount of segmented blood vessel structure, our proposed method gives the most detailed segmentation of the blood vessel tree. This is obvious when the result of our method is compared to volume rendering, where we observe that even the smallest blood vessels which are only partially visible in volume rendering are segmented using our proposed method. The results of our proposed method are nicely smoothed tubular-shaped vessels, which happens due to the radial positioning of line-shaped SEs for a single pixel. More results of segmenting the 3-D CTA images of brain blood vessels using our proposed method for different data sets are shown in figure 12.

Figure 13 shows comparison of skeletons obtained from segmentation using generalized profiles (GP) and the proposed line-shaped profiles (LP). Due to robustness to noise, the LP method yields more accurate skeletons, where the draining vein and largest arteries are easy to delineate because of high radii values. This is illustrated in the third row, where the best path between the largest vessels through the AVM are depicted. It should be noticed that the skeleton paths using the LP method represent the vessels accurately, while the best paths obtained using GP method tend to take shorter paths through vessels which are not well delineated.

### 3.3. Validation

The validation of our algorithm is performed on 4 data sets consisting of CTA images of blood vessels containing AVMs, the CTA images of blood vessels after the embolization procedure (where the AVM is no longer visible) and the CTA images of the onyx cast (glue used to occlude the AVM). To achieve quantitative validation we segment the onyx cast images by thresholding with the highest skull intensity in the image (the cast and the skull are clearly visible in CTA images). The segmented onyx is further filled-in (closed) to obtain an onyx mask. We use the obtained onyx mask to extract the AVM region from the segmented blood vessel image. Finally, in order to validate our results we compare the extracted AVM and onyx cast segmentations in table 6. It is

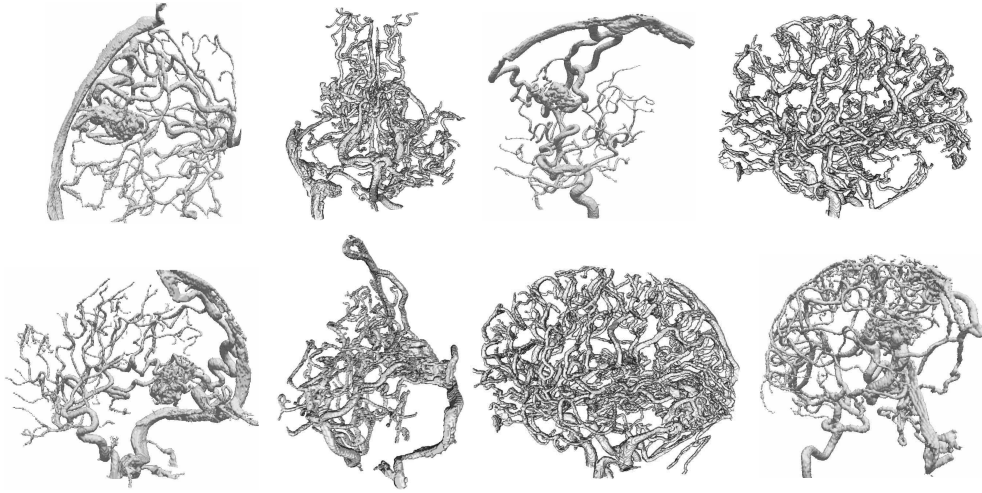


**Figure 12.** Segmentation of the blood vessel tree for different CTA data sets using our proposed method. Each segmentation result shows a nicely segmented blood vessel tree with clearly visible AVM area (where existing) with its feeding arteries and draining vein.

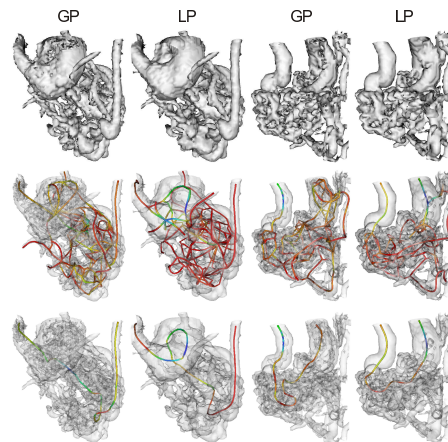


**Figure 13.** Comparison of skeletons and best paths calculated using the generalized profiles (GP) and line-shaped profiles (LP) method. The first row shows segmentation models of two AVM structures for each method. The corresponding skeletons are in the second row. The third row depicts the best paths from the vein to the arteries through the AVM. The skeleton of the LP method follows the vessels more accurately than the GP method.

important to take into account the fact that embolization procedure can deform some AVM vessels (especially in the nidus). The obtained Dice coefficient and the volume percent error values in table 6 show expected values for onyx and AVM segmentation comparisons (the Hausdorff distance was not calculated due to its high susceptibility to model deformations, which happen in AVM embolization). Figure 14 shows 2 different validation data sets with visualized segmented blood vessels, skeleton, onyx cast and extracted AVM regions. Cerebral blood vessel CTA data sets are segmented using

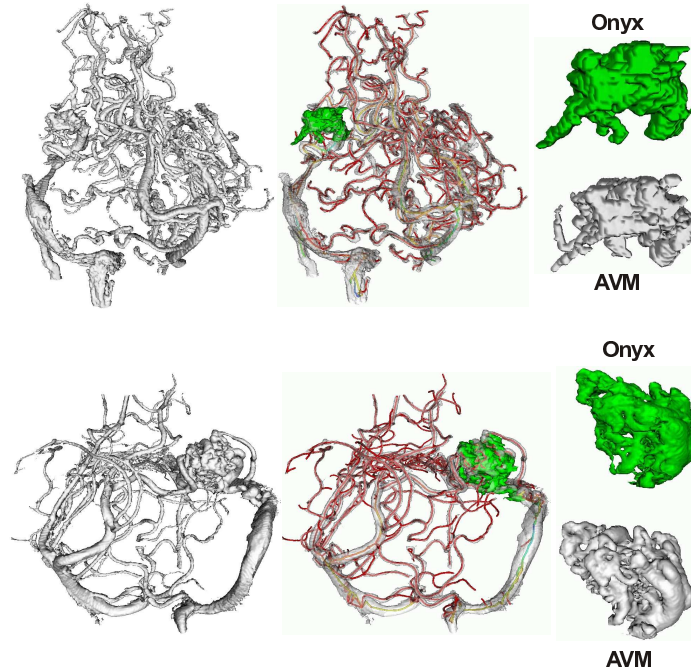


**Figure 14.** Segmentation of the blood vessel tree for 2 different CTA data sets using our proposed method. Each segmentation result shows a well segmented blood vessel tree with clearly visible AVM area with the skeleton structure clearly depicting feeding arteries and draining vein. The skeleton colour represents vessel radii, starting from blue colour for high radii values down to red colour for low radii values. The segmented onyx cast is given in green colour. The third row shows the extracted AVM segmentation region and the corresponding onyx cast segmentation.

**Table 6.** Comparisons of the segmented onyx cast with the extracted AVM segmentation

Validation	set 1	set 2	set 3	set 4
Dice	0.75	0.77	0.82	0.61
Vol. % error	6.58	12.54	10.9	10.5

our proposed algorithm. The segmented blood vessel images are skeletonized using our binary skeletonization method presented in (Babin et al. 2008), and the skeleton image is converted to a vector skeleton structure. The nodes in the vector skeleton are created from the node voxels (voxels that have more than 2 neighbours in their 26-neighbourhood) in the skeleton image by averaging the positions of all the adjacent node voxels. It can be observed that the segmented blood vessels correctly represent feeding arteries and draining vein of the AVM. The extracted AVM segmentation corresponds well to the onyx cast segmentation as depicted in the third row of figure 14.

The total computation time for a data set of 230 slices with resolution of images  $256 \times 256$  on 2GHz CPU is 2 minutes. The visualization was done using Visualization Toolkit (VTK) (Schroeder et al. 1998).

#### 4. Discussion

Our proposed algorithm works by comparing the pixel values to the characteristic values of their neighbourhoods. This segmentation principle is robust to high variety of pixel intensities, but it assumes the presence of an object in the image (the smaller the object area, the more noisy pixels get segmented, see figure 4). However, if the image consists only of noisy background (no object present in the slice), the pixels containing higher intensity noise will be segmented. This is not a significant drawback due to the fact that the slices in the original CTA images that contain only noise are rarely found and that these slices should not at all be processed. Another way to solve this problem is the application of thresholding as a preprocessing step, as shown in the block diagram in figure 6.

In some cases the difference between the highest and the lowest intensities found in blood vessels of the 3-D image is too large (sometimes the lowest intensities fall under 5% of the value of the highest intensities), and the vessels containing the lowest intensities do not get segmented. However, this happens only at poorly contrasted vessels (low quantity of contrast fluid), which are no longer at the region of interest for brain blood vessel structure analysis. On the other hand, if the low contrasted vessels need to be segmented, it can be done by setting the region of interest to contain only these vessels and applying our proposed algorithm.

We run our algorithm for profile calculation in 3-D space, which is an advantage over generalized profiling method (Babin et al. 2012) that works in slice-by-slice manner.

#### 5. Conclusion

In this work we have introduced line-shaped profiling with an application to segmentation of 3-D CTA images of brain blood vessels. The main novelty of our work is the use of line-shaped SEs, which transforms the idea of a multi-scale approach from our earlier work into a multi-orientation approach and significantly shortens execution times when compared to classical SE shapes. Another major novelty is the introduction of second order profile operators, as operators applied to sets of line-shaped SE operator values, instead of only to the elements of an individual line-shaped SE. The strength of our method comes from the use of both local proximate (close) and a wider neighbourhood of the processed pixel. The method requires only one parameter selection, which is easy to select (performed in a “threshold value selection” manner). The results on phantom data sets for various noise and artefact levels show high robustness of the proposed method. The validation performed by comparison of segmented AVM region with the segmented images of onyx cast after embolization procedure showed effectiveness of our method. The obtained results on real CTA data are nicely smoothed tubular-shaped vessels, which is a consequence of the radial positioning of line-shaped SEs for a single pixel. Our method accurately segments the highest amount of blood vessel structure compared to other segmentation methods discussed in the paper.

#### References

Antiga L & Steinman D 2006 ‘Vascular modeling toolkit’.

- Babin D, De Bock J, Pizurica A & Philips W 2008 in 'Annual Workshop on Semiconductor Advances for Future Electronics and sensors, 11th, Proceedings' STW Technology Foundation pp. 295–298.
- Babin D, Pizurica A, Bellens R, De Bock J, Shang Y, Goossens B, Vansteenkiste E & Philips W 2012 *Medical Image Analysis, Elsevier* **16**(5), 991–1002.
- Babin D, Vansteenkiste E, Pizurica A & Philips W 2009 in 'Proc. Annual Int. Conf. of the IEEE Engineering in Medicine and Biology Society EMBC 2009' pp. 4399–4402.
- Bellens R, Gautama S, Martinez-Fonte L, Philips W, Chan J C W & Canters F 2008 *IEEE Transactions on Geoscience and Remote Sensing* **46**(10), 2803–2813.
- Berger M O, Anxionnat R, Kerrien E, Picard L & S'oderman M 2008.
- Bullitt E, Aylward S, Bernard E & Gerig G 2001 *Neurosurgery* **48**, 576–583.
- Carrillo J, Orkisz M & Hoyos M 2005 in A Gagalowicz & W Philips, eds, 'Computer Analysis of Images and Patterns' Vol. 3691 of *Lecture Notes in Computer Science* Springer Berlin, Heidelberg pp. 604–611.
- Caselles V, Kimmel R & Sapiro G 1995 in 'Proc. Conf. Fifth Int Computer Vision' pp. 694–699.
- Castro M A & Cebal J R 2007 *AJNR Am J Neuroradiol* **27**, 1703–1709.
- Cebal J R, Castro M A, Appanaboyina S, Putman C M, Millan D & Frangi A F 2005 *IEEE Transactions on Medical Imaging* **24**(4).
- Coenen V, Dammert S, Reinges M, Mull M, Gilsbach J & Rohde V 2005 *International Neuroradiology, Springer Berlin* pp. 66–72.
- Coste E, Gibon D, Leclercq X, Verdonck B, Vausseur C & Rousseau J 2001 *Int. J. Radiation Oncology Biol. Phys., Elsevier* **50**(1), 247–255.
- De Bock J & Philips W 2010 *IEEE Transactions on Image Processing*. **19**, 3222–3231.
- Dice L R 1945 *Ecology* **26**(3), 297–302.
- Dokladal P, Lohou C, Perrotin L & Bertrand G 1999 'A new thinning algorithm and its application to extraction of blood vessels'.
- Forkert N, Säring D, Wenzel K, Illies T, Fiehler J & Handels H 2009 *Medical Informatics in a United and Healthy Europe, IOS Press* pp. 816–820.
- Frangi R F, Niessen W J, Vincken K L & Viergever M A 1998 Springer-Verlag pp. 130–137.
- Hoi Y, Meng H, Woodward S H, Bendok B R, Hanei R A, Guterman L R & Hopkins L N 2004 *J Neurosurg.* **101**, 676–681.
- Jackowski M, Papademetris X, Dobrucki L, Sinusas A & Staib L 2005 in J Duncan & G Gerig, eds, 'Medical Image Computing and Computer-Assisted Intervention MICCAI 2005' Vol. 3750 of *Lecture Notes in Computer Science* Springer Berlin / Heidelberg pp. 701–708.
- Kirbas C & Quek F K H 2004 *ACM Computing Surveys* **36**, 81–121.
- Lesage D, Angelini E D, Bloch I & Funka-Lea G 2009 *Med Image Anal* **13**(6), 819–845.
- Lorigo L, Faugeras O, Grimson W, Keriven R, Kikinis R, Nabavi A & Westin C F 2001 *Medical Image Analysis* **5**(3), 195–206.
- Nain D, Yezzi A & Turk G 2004 in 'Proceedings of MICCAI, St. Malo, France'.
- Okada T, Miki Y, Kikuta K, Mikuni N, Urayama S, Fushimi Y, Yamamoto A, Mori N, Fukuyama H, Hashimoto N & Togashi K 2007 *AJNR Am J Neuroradiol* **28**, 1107–1113.
- Papademetris X, Jackowski M, Rajeevan N, Okuda H, Constable R & Staib L n.d. 'Bioimage suite: An integrated medical image analysis suite'.
- Passat N, Ronse C, Baruthio J, Armspach J P & Maillot C 2006 *Medical Image Analysis* **10**(2), 259–274.
- Passat N, Ronse C, Baruthio J, Armspach J P, Maillot C & Jahn C 2005 *Journal of Magnetic Resonance Imaging* **21**(6), 715–725.
- Pechaud M, Keriven R & Peyre G 2009 in 'Computer Vision and Pattern Recognition, 2009. CVPR 2009. IEEE Conference on' pp. 336–342.
- Pesaresi M & Benediktsson J A 2001 *IEEE Transactions on Geoscience and Remote Sensing* **39**(2), 309–320.
- Piccinelli M, Veneziani A, Steinman D A, Remuzzi A & Antiga L 2009 *IEEE Transactions on Medical Imaging* **28**(8), 1141–1155.
- Pieper S, Lorensen B, Schroeder W & Kikinis R 2006 in 'Biomedical Imaging: Nano to Macro, 2006. 3rd IEEE International Symposium on' pp. 698–701.
- Plaza A, Martinez P, Perez R & Plaza J 2004 *Pattern Recognition, Elsevier* **37**, 1091–1116.
- Qian X, Brennan M, Dione D, Dobrucki W, Jackowski M, Breuer C, Sinusas A & Papademetris X 2009 *Medical Image Analysis* **13**(1), 49–61.
- Säring D, Fiehler J, Forkert N, Piening M & Handels H 2007 *International Journal of Computer Assisted Radiology and Surgery* **2**, 75–79.
- Schroeder W, Martin K M & Lorensen W E 1998 *The visualization toolkit (2nd ed.): an object-*

- oriented approach to 3D graphics* Prentice-Hall, Inc.
- Shang Y, Deklerck R, Nyssen E, Markova A, de Mey J, Yang X & Sun K 2011 *IEEE Transactions on Biomedical Engineering* **58**(4), 1023–1032.
- Shang Y, Yang X, Zhu L, Deklerck R & Nyssen E 2008 *Computerized Medical Imaging and Graphics, Elsevier* **32**(2), 109–117.
- Söderman M, Karlsson B, Launnay L, Thuresson B & Ericson K 2000 *Neuroradiology*, Springer-Verlag **42**, 697–702.
- Wesarg S & Firlé E A 2004 in 'Proceedings of SPIE The International Society for Optical Engineering' Vol. 3 pp. 1609–1620.
- Yaniv Z & Cleary K 2006 *Computer Aided Interventions and Medical Robotics*.
- Zhang X, Shirato H, Aoyama H, Ushikoshi S, Nishioka T, Zhang D & Miyasaka K 2003 *Int. J. Radiation Oncology Biol. Phys., Elsevier* **57**(5), 1392–1399.